# Energetics and migration of point defects in $Ga_2O_3$

Miguel A. Blanco,* Munima B. Sahariah,† Huitian Jiang, Aurora Costales,‡ and Ravindra Pandey
*Department of Physics, Michigan Technological University, Houghton, Michigan 49931, USA*
(Received 19 July 2005; revised manuscript received 26 September 2005; published 16 November 2005)

The results of a theoretical study on the point defects of monoclinic $\beta$-$Ga_2O_3$ are reported here. The point defects considered here are vacancies, interstitials together with dopant ions such as Be, Mg, In, Cr, Si, Ge, Sn, and Zr. Since the low symmetry of the monoclinic lattice does not provide an unambiguous location of interstitial sites and migration paths, we propose a unique way for their identification in terms of the electron density topology. Special attention has also been given to the preference among the lattice and interstitial sites for the impurity defects, and its explanation in terms of structural, electrostatic, and electron density arguments. The calculated results find the most prominent features in the lattice to be the existence of (i) empty channels along the **b** direction, and (ii) atomic layers perpendicular to them. Their interplay governs the stability and mobility of the point defects in $\beta$-$Ga_2O_3$. The anionic Frenkel pair consisting of the oxygen vacancy and oxygen interstitial is predicted to dominate the defect structure in the lattice. The dopants considered here are likely to be stabilized at the octahedral gallium sites, except for $Be^{+2}$, which prefers a tetrahedral gallium site in the lattice. Some of the possible migration paths have been determined, and the pseudoactivation energies for the intrinsic, oxygen-rich, and oxygen-deficient conditions are computed as a function of temperature. It is suggested that tuning the concentration of oxygen can lead to a change in the anisotropy of the ionic conductivity in $\beta$-$Ga_2O_3$.

DOI: 10.1103/PhysRevB.72.184103 PACS number(s): 61.72.Ji, 66.30.−h, 66.30.Lw, 68.55.Ln

## I. INTRODUCTION

Thin films and single crystals of gallium oxide ($Ga_2O_3$) have acquired an increasing importance in recent years because of their diverse applications in various technologically important fields. For example, $Ga_2O_3$ is useful in the fabrication of masers,[1] metal-insulator structures, facet coatings of semiconducting lasers,[2–5] and field-effect devices.[6] The applicability of $Ga_2O_3$ for switching memory devices[7,8] was suggested by a bistable Overhauser effect observed in the conduction electron spin resonance measurements. It is also considered as a pioneer material in a new family of transparent conducting oxides (TCOs), especially for transmitting UV light.[9–11] Since TCOs are the key to optoelectronic devices and solar cells, many experimental studies[12–17] have been devoted to conventional and low-dimensional properties of the material. It has also drawn attention for its promising potential in ultra-sensitive gas-detecting devices.[18,19] In particular, the gas sensors based on polycrystalline films of $\beta$-$Ga_2O_3$ have shown very stable operating characteristics at high temperatures. With an ability to detect different gases depending on the environment, $\beta$-$Ga_2O_3$ is expected to have a wide range of applications in the automobile industry.

At ambient conditions, $Ga_2O_3$ occurs in the monoclinic (i.e., $\beta$) phase, although it can be transformed into four other high-pressure and temperature polymorphs.[1,20,21] The monoclinic phase has $C2/m$ symmetry with four formula units per crystallographic cell.[22–24] In the lattice unit cell, there are two crystallographically nonequivalent Ga atoms, and three nonequivalent O atoms. The local symmetry of the constituent atoms is $C_s$, and Ga atoms have tetrahedral- and octahedral-like coordination in the lattice. $\beta$-$Ga_2O_3$ is found to be an intrinsic insulator, with a band gap of 4.9 eV,[25,26] although it displays a semiconducting behavior when synthesized in reducing conditions.[27–29] The dc and ac conductivity measurements in single crystals of $\beta$-$Ga_2O_3$ show that the dominant mechanism for migration below 900 K is ionic due to diffusion of oxygens in the lattice. Above 900 K, the conductivity is predominantly electronic.[30]

The photoluminescence studies on single crystals of $\beta$-$Ga_2O_3$ reveal three dominant bands in the ultraviolet (UV), blue, and green regions of the emission spectrum.[31] The UV emission is an intrinsic phenomenon attributed to the recombination of an electron and a self-trapped hole.[32] However, the blue and green emissions are found to occur only in the presence of specific impurities, such as Be, Ge, Zr, and Si, in the lattice.[8]

In spite of the availability of numerous experimental studies on point defects in $Ga_2O_3$, there is very little understanding of the energetics of native defects and dopants in the lattice. Surprisingly, there is also a complete dearth of theoretical studies on $Ga_2O_3$, and, in fact, on low-symmetry crystals in general. This may be because the low symmetry makes theoretical studies of point defects to be expensive in terms of computational resources, but also due to the unambiguity in the determination of the interstitial sites and the migration paths.

In this paper, we report the results of a comprehensive theoretical study of point defects in $\beta$-$Ga_2O_3$. Specifically, we will focus on defect energetics and diffusion of host-lattice and dopant ions in the lattice, paying attention to the ionic conductivity, in the framework of the shell model. First, we will develop a set of shell-model pair potentials to describe interactions involving the constituent ions and dopants in the lattice. Using the shell model description of the lattice, defect energetics, and site preferences for dopants will be calculated. We will also study several migration paths for ions in the lattice, calculating the concentration and temperature dependence of the pseudoactivation energies for migra-

 

tion. Since $\beta$-$Ga_2O_3$ is the only monoclinic metaloxide that is stable from room temperature to its melting point,[18,33] we believe that this endeavor will also open the door for further theoretical studies on materials of this type in the near future.

The paper is organized as follows. In the next Section we describe the shell model, and the derivation of the interionic potentials. The calculated results pertaining to native defects and dopants in $\beta$-$Ga_2O_3$ are presented and discussed in Sec. III. We provide a summary in Sec. IV. The derivation of some of the equations used in this paper is given in the Appendix.

## II. THEORETICAL METHOD

### A. Model

The simulation of ionic oxides using interatomic potentials is now a well established field with the most common approach being based on a fully ionic description of such materials.[34] Even beyond this, the ionic model is often found to be a reasonable basis for interatomic potential models as any effects of covalency can be subsumed into the parametrization for closed shell ions, such as those being considered in this study. Based on the difference in electronegativity of Ga and O, the metal-oxygen bond in $\beta$-$Ga_2O_3$ is mainly expected to be an ionic bond. It therefore allows us to choose a fully ionic description of the constituent ions in the lattice with an assignment of the nominal charges of +3 and −2 to gallium and oxygen, respectively.

Due to the low lattice symmetry, and the charged constituent ions, an adequate representation of the lattice polarization is foreseen to play a major role in the simulation study of $Ga_2O_3$. Thus, we have chosen a dipolar shell model[34] to describe the interionic interactions in the lattice. In this model, we use central-force interionic potentials, in which contributions of the overlap repulsion and dispersion forces, between ions $i$ and $j$ at separation $r_{ij}$, are described by a short-range Buckingham-type potential,

$$V_{ij}^{sr}(r_{ij}) = A_{ij}e^{-r_{ij}/\rho_{ij}} - \frac{C_{ij}}{r_{ij}^6}. \tag{1}$$

Here, $A_{ij}$ is the pre-exponential constant for the overlap repulsion potential with hardness parameter $\rho_{ij}$. $C_{ij}$ is the constant for the average dipole-dipole van der Waals interaction, which typically accounts for long-range attraction between closed shell anions. On the other hand, long-range electrostatic interactions are described by the Coulomb law,

$$V_{ij}^{\mathrm{Coul}}(r_{ij}) = \frac{q_i q_j}{r_{ij}}, \tag{2}$$

where $q_i$ and $q_j$ are the ionic charges of ions $i$ and $j$, respectively. The conditionally convergent sum of this Coulomb interaction in an infinite lattice is carried on by the Ewald technique, whereas the sum of the short-range interactions is carried up to a cutoff of 16 Å.

To account for the ionic polarization, the shell model assumes the ions to be formed by a shell of charge $Y_i$, which is responsible for the short-range interionic interactions, and a core, which carries the rest of the ionic charge and does not interact with the rest of the lattice via short-range interactions. The core and its shell are, however, linked by a springlike interaction of the form

$$V_{\text{core-shell}}(r) = \frac{1}{2}k_2 r^2 + \frac{1}{24}k_4 r^4, \tag{3}$$

where $k_2$ and $k_4$ are spring constants and $r$ is the core-shell separation. The charge separation model (i.e., core and shell) accounts for the ionic dipole, while the springlike interaction term represents the ionic polarizability. The anharmonic term in Eq. (3) is generally added to avoid the so-called overpolarization effects in some highly strained defect calculations.

Calculations of point defects are based on a physical model devised by Mott and Littleton.[34] Here, the lattice containing the defect is divided into three concentric regions that are treated with decreasing levels of accuracy: region 1, comprising the defect and a few shells around it; region 2a, which surrounds region 1 and is larger in size; and region 2b consisting of the rest of the lattice. Thus, region 2b is treated as a dielectric continuum, and the polarization effects due to the net charge of the defect are calculated by a partial transformation into reciprocal space. On the other hand, both region 1 and region 2a are combined in a consistent way but with the displacements and polarizations evaluated differently. In region 1, ions are treated explicitly at the atomistic level and are allowed to relax completely. The ions in region 2a are also allowed to relax, but only in a restricted manner: they are assumed to provide a harmonic response to the force field arising due to the defect, which is only true if we consider that the perturbation introduced by the defect in the lattice is weak. This assumption consequently requires that the region 1 should be large enough to contain most of the perturbation introduced by the defect in the lattice. Our previous studies on a wide variety of complex materials including oxides,[35] nitrides,[36] and chalcopyrites[37] suggest that approximately 500 ions in region 1 are adequate enough to meet this criterion. In this study, we have fixed the radius of region 1 at 9 Å, which encompasses about 550 ions. The electrostatic force of region 1, screened by the dielectric constant, is then employed to calculate the displacements in region 2a.

For the bulk and defect calculations in $\beta$-$Ga_2O_3$, we have used the GULP program,[38] which has been successfully employed in several atomistic simulation studies of ionic and semi-ionic materials. The main features of GULP include a highly efficient energy minimization technique that uses first and second derivatives and reliable symmetry simplifications, which is a prerequisite for any subsequent evaluation of the physical properties of a defect-free or defect-containing crystal.

### B. Interionic potentials: Host lattice

The host-lattice interionic potentials involving O-O and Ga-O ions were obtained by fitting the potential parameters (i.e., $A$, $\rho$, $C$, $Y$, $k_2$, and $k_4$) to the known bulk properties of $\beta$-$Ga_2O_3$. The interaction involving the second-neighbor Ga-Ga ions is assumed to be weak and is neglected. The Ga ions are also assumed to be rigid ions in the lattice.

TABLE I. Short-range potential and shell-model parameters for $\beta$-$Ga_2O_3$ [see Eqs. (1) and (3)]. The Ga ions in the lattice are taken to be rigid ions, and the second-neighbor Ga-Ga interaction is assumed to be weak and is neglected in the derived parameter set.

(a) Shell-shell interactions

| | $A_{ij}$ (eV) | $\rho_{ij}$ (Å) | $C_{ij}$ (eV Å$^6$) |
|---|---|---|---|
| $Ga_s$-$O_s$ | 907.89 | 0.345 | 10.0 |
| $O_s$-$O_s$ | 22764.0 | 0.149 | 0.0 |

(b) Core-shell interactions

| | $k_2$ (eV Å$^{-2}$) | $k_4$ (eV Å$^{-1}$) | $Y(e)$ |
|---|---|---|---|
| $Ga_c$-$Ga_s$ | 15.26 | 10000 | 2.67 |
| $O_c$-$O_s$ | 74.92 | 10000 | −2.51 |

The fitting procedure is a multidimensional, nonlinear, square root deviation minimization procedure, for which the starting potential parameters may play a crucial role. We have therefore started the fitting procedure with the $O^{-2}$-$O^{-2}$ short-range potentials of Catlow *et al.*,[39] suitable for a wide range of binary oxides, and $A$ and $\rho$ of $Ga^{+3}$-$O^{-2}$ from Pandey *et al.*[35] developed for $ZnGa_2O_4$. The shell charges ($Y$) and spring constants ($k_2$ and $k_4$) for Ga and O are then fitted to reproduce dielectric properties of the lattice. After the initial fitting, a more complex relaxed fitting procedure was employed in which the least square sum was defined by the experimental lattice geometry, the bulk modulus, and static and high-frequency dielectric constants. The crystal structure was then optimized for each set of potential parameters, computing the actual variation in the structural parameters rather than the estimated gradient at the experimental geometry. This is a much superior strategy: while allowing the structure to change according to the potential parameters, it makes them sensitive to the lattice geometry, so that the fitted parameters are also those that give an overall better optimized lattice structure as well as crystal properties. The final interionic potential parameters obtained through this procedure are given in Table I. Table II lists both experimental and computed lattice properties generated by the derived parameter set for $\beta$-$Ga_2O_3$.

### C. Interionic potentials: Dopants-oxygen

In order to obtain the lattice-adapted interionic potentials for dopant ions in $\beta$-$Ga_2O_3$, *ab initio* perturbed ion[40,41] ionic descriptions of dopant and host-lattice ions were used here following the lines of Refs. 41–43. Accordingly, we will consider the ionic description of $O^{-2}$ at the experimental lattice geometry. For the dopant ions, we have taken *in vacuo* ionic descriptions, since the electronic distributions of positively charged ions are not expected to change significantly upon their incorporation into the lattice. In the *ab initio* perturbed ion calculations, the multizeta Slater-type basis sets of Clementi and Roetti[44] were used for oxygen and dopant cations, namely $Be^{+2}$, $Mg^{+2}$, $In^{+3}$, $Cr^{+3}$, $Si^{+4}$, $Ge^{+4}$, $Sn^{+4}$, and $Zr^{+4}$. The resulting *ab initio* perturbed ion short-range potentials along with the host-lattice $Ga^{+3}$-$O^{-2}$ potential are shown in Fig. 1, and Table III collects the values of the respective parameter sets (i.e., $A$ and $\rho$). In defect calculations, the dopant ions are considered as rigid ions and the second-neighbor dopant-Ga interaction is ignored.

TABLE II. Bulk properties of $\beta$-$Ga_2O_3$. In the unit cell of the monoclinic phase with the $C2/m$ space group, there are inequivalent Ga (2) and O (3) atoms located at $4i$ $(x,0,z)$ with $C_s$ symmetry.

| Property | Exp. | Calc. | Property | Exp. | Calc. |
|---|---|---|---|---|---|
| Lattice parameters | | | Fractional coordinates | | |
| $a$(Å) | 12.23 | 12.14 | $x_{Ga_I}$ | 0.0904 | 0.0887 |
| $b$(Å) | 3.04 | 3.14 | $z_{Ga_I}$ | 0.7948 | 0.7976 |
| $c$(Å) | 5.80 | 5.85 | $x_{Ga_{II}}$ | 0.3414 | 0.3457 |
| $\beta$(degree) | 103.7 | 103.7 | $z_{Ga_{II}}$ | 0.6857 | 0.6869 |
| Avg nearest-neighbor distance | | | $x_{O_I}$ | 0.1674 | 0.1509 |
| $Ga_I$-$R_{nn}$(Å) | 1.83 | 1.83 | $z_{O_I}$ | 0.1011 | 0.1119 |
| $Ga_{II}$-$R_{nn}$(Å) | 2.01 | 2.03 | $x_{O_{II}}$ | 0.4957 | 0.4887 |
| $O_I$-$R_{nn}$(Å) | 1.92 | 1.91 | $z_{O_{II}}$ | 0.2553 | 0.2554 |
| $O_{II}$-$R_{nn}$(Å) | 1.87 | 1.87 | $x_{O_{III}}$ | 0.8279 | 0.8247 |
| $O_{III}$-$R_{nn}$(Å) | 2.01 | 2.05 | $z_{O_{III}}$ | 0.4365 | 0.4279 |
| Bulk modulus | | | Dielectric constants | | |
| $B_0$(GPa) | 200 | 197 | $\epsilon_0$ | 10.2 | 11.8 |
| | | | $\epsilon_\infty$ | 4.71 | 3.35 |

## III. RESULTS AND DISCUSSION

### A. Native defects: Vacancy and interstitial

Even an undoped crystal can have point defects referred to as native defects. These include vacancies, interstitials, and antisites. In the present case, antisites are quite unlikely to form in the lattice due to its highly ionic nature. We will therefore focus on vacancies and interstitials in this study. To preserve the stoichiometry of the lattice, defects generally appear in definite combinations, such as Frenkel or Schottky defects. The Schottky defects in the lattice are formed by moving the constituent ions to the surface from their bulk sites. On the other hand, the Frenkel defects are pairs of vacancies and interstitials of the same type of ion. The low symmetry of the $\beta$-$Ga_2O_3$ lattice allows several possible vacancies and interstitial defect sites for both Ga and O in the lattice. We therefore first discuss the formation energies of individual defects before discussing the energetics of Frenkel or Schottky defects in $\beta$-$Ga_2O_3$.

#### *1. Vacancies*

Table IV lists the values of the formation energy of Ga and O vacancies. We label Ga ions occupying tetrahedral and octahedral sites as $Ga_I$ and $Ga_{II}$, respectively. The oxygen ions that are labeled as $O_I$, $O_{II}$, and $O_{III}$ have coordination indices of 3, 3, and 4, respectively. Since the formation energy of a vacancy is defined as that required to remove a lattice ion to infinity, the ordering of the calculated formation energies of Ga and O vacancies can be understood in terms of the electrostatic potential at the given site. The most fa-

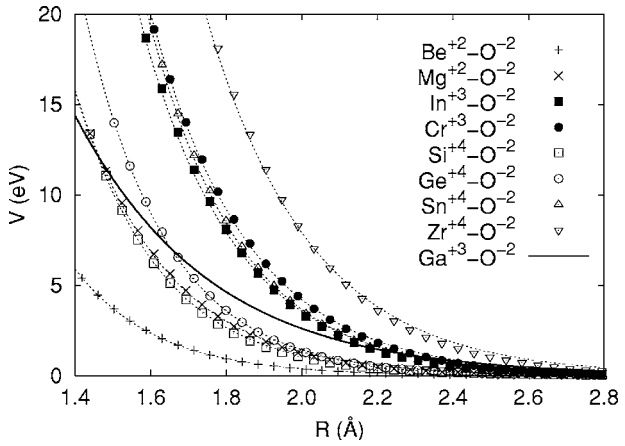


FIG. 1. *Ab initio* perturbed ion interionic potentials for the dopant-oxygen interactions in $\beta$-$Ga_2O_3$. Symbols correspond to computed values, dotted lines correspond to the fitted curves. The solid line corresponds to the Ga-O interionic potential in $\beta$-$Ga_2O_3$.

vored vacancy is expected to be associated with the atom, which has the smaller stabilization contribution given by $q\phi$, where $\phi$ is the electrostatic potential. For example, the calculated electrostatic potentials at $O_I$, $O_{II}$, and $O_{III}$ sites are 25.20, 26.09, and 24.56 V, respectively, indicating the preference for $V_{O_{III}}$ in the lattice. Similarly, the calculated electrostatic potential at the tetrahedral site ($\phi_{Ga_I}=-35.14$ V) is lower than that at the octahedral site ($\phi_{Ga_{II}}=-35.04$ V) in the lattice.

In fact, the calculated values of the formation energy are related to each other: the $\Delta E_f/q\phi$ quotient is 0.506 and 0.496 for $Ga_I$ and $Ga_{II}$, respectively. The quotient is 0.424, 0.423, and 0.428 for $O_I$, $O_{II}$, and $O_{III}$, respectively. In the quotient, $\Delta E_f$ is the defect formation energy taken from Table IV. The $\Delta E_f/q\phi$ quotient therefore shows, especially for oxygens, that even though the loss of the electrostatic contribution is only a part of the total vacancy formation energy, the missing short-range interactions and the vacancy relaxation contributions are closely related to the electrostatic forces, to the point of being almost proportional to them. Finally, it is also to be noticed that the values of $\Delta R_{nn}$ given in Table IV are all positive, indicating an outward relaxation of the neighboring ions of the vacancies. This is as would be expected, since the removal of a lattice atom with a charge opposite to that of its neighbors introduces a large repulsion among them. This is further reinforced by the coordination index of the vacancy site shown in Table IV. The coordination index of $Ga_I$, $O_I$, and $O_{III}$ vacancy sites has decreased with respect to that of the perfect lattice. Although the $Ga_{II}$ and $O_{II}$ vacancies maintained their co-ordination polyhedra, near neighbors were found to relax outwardly in the lattice due to their electrostatic repulsion.

### *2. Interstitials*

In a high symmetry lattice, such as NaCl, the most likely positions of interstitials can easily be identified. There usually exist unoccupied high-symmetry Wyckoff positions of the corresponding space group, that are sites with fixed coordinates. It is then easy to locate, by simple inspection, a favorable coordination for any interstitial ion among these unoccupied sites, using the electrostatic potential (necessarily a critical point) as a guidance. However, low symmetry lattices offer no such guidance in identifying the interstitial positions in the lattice: they usually contain few or no fixed coordinate appropriate Wyckoff positions, and the electrostatic potential does not necessarily display further maxima or minima than the ionic positions. This is indeed the case for the $\beta$-$Ga_2O_3$ lattice, and hence some criterion is needed to select candidate interstitial positions.

We begin with the observation that the appropriate interstitial sites in an ionic lattice can be located from the extrema of the point-charge electrostatic potential (see Fig. 2). This is due to the fact that positions with a maximum of the potential will stabilize anions, while minima of the potential will stabilize cations. Following this guidance, the interstitial sites in a high-symmetry lattice can be correctly located, e.g., the potential at an octahedral site in the NaCl lattice is a maximum or minimum, due to the high symmetry of the corresponding Wyckoff position. However, the above-mentioned guidance may fail for a low-symmetry lattice, since a similar octahedral-like site may not show a maximum or a minimum of the potential at all. Even if the maxima or minima of the potential are present in a low-symmetry crystal, they may be quite difficult to locate in a lattice that has much sharper maxima and minima of the potential at the anionic and cationic sites. For example, the potentials are generally of the order of +25 V for the anionic site and −35 V for the cationic site, while the interstitial sites are expected to be associated with potentials of the order of tenths of V.

In this study, we propose that a much better guidance can be obtained in locating interstitial sites in a low symmetry lattice when attending to the topology of the electron density, $\rho(\mathbf{r})$. The electron density is a positive definite function, which peaks at the nuclei and decays exponentially in going away from the nuclei. Thus, the minima of $\rho$ are sites with a smaller short-range repulsion (e.g., steric interaction), and are therefore good candidates for interstitial sites. The electrostatic potential on each site can help in determining if the position is more suitable for an anion or a cation interstitial. Another advantage is that obtaining the topology of $\rho$ can be automated,[45] thus providing a guide in low-symmetry lattices. Since these lattice positions are only tentative interstitial sites, which will be ultimately optimized during energy minimization of the defective lattice, and the topology is fairly insensitive to the method used to obtain $\rho$, almost any well-behaved electron density can serve to provide the guid-

TABLE III. *Ab initio* perturbed ion short-range potential parameters for the dopant-oxygen interactions in $\beta$-$Ga_2O_3$.

| Pair | $A_{ij}$ (eV) | $\rho_{ij}$ (Å) | Pair | $A_{ij}$ (eV) | $\rho_{ij}$ (Å) |
|---|---|---|---|---|---|
| $Be^{+2}$-$O^{-2}$ | 3633.0 | 0.2179 | $Si^{+4}$-$O^{-2}$ | 8030.2 | 0.2246 |
| $Mg^{+2}$-$O^{-2}$ | 5214.9 | 0.2413 | $Ge^{+4}$-$O^{-2}$ | 14 165.4 | 0.2173 |
| $In^{+3}$-$O^{-2}$ | 10 591.9 | 0.2500 | $Sn^{+4}$-$O^{-2}$ | 15 050.7 | 0.2403 |
| $Cr^{+3}$-$O^{-2}$ | 10 323.7 | 0.2562 | $Zr^{+4}$-$O^{-2}$ | 11 461.0 | 0.2748 |

TABLE IV. Formation energy ($\Delta E_f$), variation (percentage) in the average nearest-neighbor distance ($\Delta R_{nn}$), and coordination index ($I_c$) of vacancies in $\beta$-$Ga_2O_3$. The average $R_{nn}$ in the perfect lattice is given in Table II.

| Defect | $\Delta E_f$ (eV) | $\Delta R_{nn}$ (Å) | $I_c$ |
|---|---|---|---|
| $V_{Ga_I}$ | 53.3 | +0.46 (25%) | 3 |
| $V_{Ga_{II}}$ | 52.2 | +0.46 (23%) | 6 |
| $V_{O_I}$ | 21.4 | +0.38 (20%) | 2 |
| $V_{O_{II}}$ | 22.1 | +0.46 (25%) | 3 |
| $V_{O_{III}}$ | 21.1 | +0.31 (15%) | 3 |

ance. In the present study, we rely on the electron density computed through the *ab initio* perturbed ion (*ai*PI) method,[41] which was previously used to generate the interionic potentials for dopants in $\beta$-$Ga_2O_3$.

Several candidate interstitial sites are then obtained by using the CRITIC[45] program's automatic location of critical points of the *ai*PI electron density, which are given in Table V. The first six positions are symmetry-fixed stationary points of $\rho$, but only Wyckoff position $2c$ is a true minimum. Positions $2b$, $2d$, $4e$, and $4f$, correspond to minima along the O-O direction, but maxima in the rest, and are therefore second-order saddle-points of $\rho$, referred to as bond points. Since the first six positions correspond to high-symmetry positions, they may be preferred by an interstitial or they may act as saddle points during the migration of an interstitial in the lattice. Finally, the last four positions, $i_7$, $i_8$, $i_9$, and $i_{10}$, correspond to the true, nonconstrained minima of $\rho$, and hence are good candidate sites for interstitial ions. However, there is an $i_{10}$ minimum of the electron density above and below $i_1$ along the **b** axis, and very close to it. Hence, it may happen that the stable position for the interstitial turns out to be the high symmetry position, even though it is a saddle point of $\rho$.

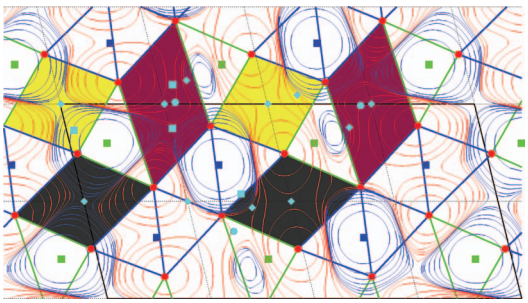

FIG. 2. (Color) Isolines of the point-charge electrostatic potential of the $\beta$-$Ga_2O_3$ lattice ($y=0$ plane, logarithmic scale, blue for positive and zero potential, red lines for negative potential). The projection of the unit cell edges and some auxiliary lines ($x=0,1/4,1/4,3/2,1$ and $z=0,1/2,1,3/2$) are drawn in black. Tetrahedral (green) and octahedral (blue) Ga sites and their coordination polyhedra are shown, with the lattice O atoms in red. Cyan symbols correspond to interstitial positions, either symmetry-fixed (diamonds), oxygen (circles), or gallium (squares). Empty channels along the $(0,y,0)$ (yellow), $(0,y,1/2)$ (black), and $(1/4,y,0)$ (red) directions are shaded in color. Lattice atoms in the plane can be recognized by the circular pattern of the isolines, those out of plane are at the $y=1/2$ parallel plane (both $y=0$ and $y=1/2$ are symmetry planes containing half the atoms in the unit cell). Due to the $C$ nature of the Bravais lattice, the $(x,1/2,z)$ points appear here as $(x+1/2,0,z)$, hence the two different instances of each channel representing the $y=0$ (left) and $y=1/2$ (right) planes. All interstitial sites shown are in the $y=0$ plane except for the $4e$ and $4f$ positions (center of red channel and middle of two octahedra, respectively), which are at $y=\pm 1/4$.

All of the minima of $\rho$ are found to be located along three channels lying parallel to the $y$ axis, which are shown in Fig. 2. These channels are colored in yellow, black, and red, showing the unique $y=0$ plane that contains all of the inequivalent atoms, and also most candidate interstitial positions (except for the interlayer $i_5$ and $i_6$). The $y=1/2$ layer is equivalent to the $y=0$ layer, although displaced $1/2$ along the **a** axis. These straight channels do not have any occupied lattice site, and thus are likely to play an important role in the study of interstitial-mediated ionic conductivity in $\beta$-$Ga_2O_3$. Along the center of each channel, the electrostatic potential is periodic, as shown in Fig. 3, suggesting the possibility of several interstitial positions. The extrema of these lines are at $y$ equal to 0 and $1/2$ for yellow and black, and the same plus $1/4$ for the red channel, favoring interstitials within the atomic layers. On the other hand, the distance to the nearest ions for an atom traveling along the center of each channel gives an indication of how large the short-range repulsion effects will be. This is shown in Fig. 4, and it seems that the short-range effects favor interlayer situations, close to the $y=0$ layer in the yellow and black channels and at the $y=1/4$ for the red channel. Thus, a competition among the short-range and the electrostatic effects appears.

To perform geometry optimization calculations of the defect-containing lattice, we start from the initial positions of interstitials given in Table V. In contrast to what we have found for vacancies, $\Delta E_f/q\phi$ varies significantly when we choose the value of $\phi$ from the unrelaxed (i.e., initial) position or from the relaxed (i.e., optimized) position. The variation, therefore, shows that the short-range repulsion effects from the neighboring ions are crucial in selecting the optimal interstitial position, supporting the proposed criterion based on electron-density minima. Moreover, from Figs. 2, 4, and 5, we see that the red channel, being the widest channel, is most likely to accommodate an interstitial in the $\beta$-$Ga_2O_3$ lattice.

Table VI collects the results for the interstitial oxygen in $\beta$-$Ga_2O_3$. We note here that the interstitial formation energy is the energy required to bring an ion from infinity to an interstitial site with the corresponding relaxation of the surrounding lattice. Based on the magnitude of the formation energy, the oxygen interstitial sites along the red channel are found to be the most stable, as expected; $i_9$ is the absolute minimum, closely followed by the symmetry-fixed $i_5$ position. The $i_9$ position was indeed the absolute minimum for the electron density, suggesting a small short-range repulsion due to neighboring ions. Although the calculated electrostatic potential at $i_9$ was negative, it was much smaller in absolute value than that of the $i_5$ position. In fact, all of the positive potential sites, which are candidate sites for a negative interstitial ion, showed shorter Ga-O and O-O distances, leading to larger short-range repulsions. In the optimized geometry,

TABLE V. Interstitial sites considered for defect calculations in $\beta$-$Ga_2O_3$. These sites are classified in terms of the color coded channels in the lattice.

| Site | Position | Coordinates | Channel | $\phi$ (V) | $\rho$ ($e$/Å$^3$) | Environment/$R_{nn}$ (Å) |
|---|---|---|---|---|---|---|
| $i_1$ | 2*a*, $C_{2h}$ | (0,0,0) | yellow | +0.285 | 0.018 | 2 Ga (1.78), 6 O (1.79–2.20) |
| $i_2$ | 2*b*, $C_{2h}$ | (0,0.5,0) | yellow | −4.520 | 0.051 | 6 O (1.53–2.38), 6 Ga (2.29–2.37) |
| $i_3$ | 2*c*, $C_{2h}$ | (0,0,0.5) | black | +0.231 | 0.009 | 2 Ga (1.82), 6 O (2.07–2.11) |
| $i_4$ | 2*d*, $C_{2h}$ | (0,0.5,0.5) | black | −7.314 | 0.095 | 2 O (1.40), 6 Ga (2.38–2.40) |
| $i_5$ | 4*e*, $C_i$ | (0.25,0.25,0) | red | −3.066 | 0.024 | 2 O (1.69), 2 Ga (2.18) |
| $i_6$ | 4*f*, $C_i$ | (0.25,0.25,0.5) | — | −2.601 | 0.142 | 4 O (1.34–2.43), 2 Ga (1.60) |
| $i_7$ | 4*i*, $C_s$ | (0.076,0.5,0.046) | yellow | −0.745 | 0.028 | 3 Ga (1.63–2.17), 4 O (1.75–1.81) |
| $i_8$ | 4*i*, $C_s$ | (0.098,0.5,0.532) | black | −1.057 | 0.026 | 3 Ga (1.59–2.23), 4 O (1.81–1.83) |
| $i_9$ | 4*i*, $C_s$ | (0.317,0,0.121) | red | −0.006 | 0.007 | 2 Ga (1.94), 4 O (2.01–2.18) |
| $i_{10}$ | 4*g*, $C_s$ | (0.0,0.039,0.0) | yellow | +0.221 | 0.018 | 2 Ga (1.78), 4 O (1.80–2.28) |

$O_{i_9}$ gets displaced in such a way that it is able to bond not only to the tetrahedral $Ga_I$ ions above and below but also to $Ga_I$ and $Ga_{II}$ in the same plane, acquiring a four-fold coordination. The resulting configuration consists of a trigonal pyramid with $O_{i_9}$ at the center of the base. The average distance between $O_{i_9}$ and the Ga neighbors (2.07 Å) is close to that of the perfect lattice (1.94 Å). The $O_{i_9}$ interstitial pushes the nearby $O_I$ ion into the neighboring yellow channel, where it forms an extra bond to a tetrahedral $Ga_I$. We label as complex defects the sites where large bond reorganizations occur. In this context, bonding is related to the interatomic distance as compared to the lattice spacing.

The next low-energy site comes out to be $i_5$, which is again in the red channel. It pushes two $O_I$ ions in a similar manner, while having a rhombus-planar coordination with two $Ga_I$ at 1.86 Å and two $Ga_{II}$ at 2.44 Å. In fact, it can be shown that the $O_{i_5}$ defect corresponds to a first-order saddle point, a maximum for the displacement of $O_i$ along the red channel between two symmetric $O_{i_9}$ positions. Since $O_{i_5}$ is at a center of symmetry, the symmetry-constrained optimization leads to the minimum along all other degrees of freedom, which turned out to be a saddle point with a negative Hessian eigenvalue.

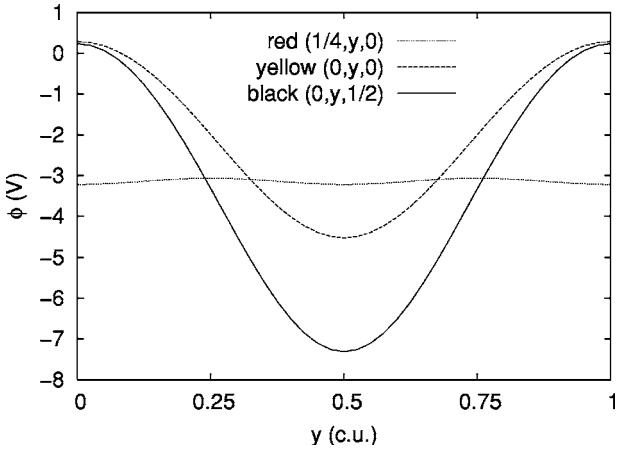


FIG. 3. Electrostatic potential along the central axis of each of the three channels defined in Fig. 2.

The interstitial positions along the yellow channel are predicted to be associated with a high formation energy, $O_{i_{10}}$ being the lowest among them. Although the initial $i_{10}$ almost coincides with $i_1$, its final optimized position reaches an almost tetrahedral coordination with a very small lattice distortion at a position intermediate between $i_1$ and $i_2$. In fact, these two high-symmetry positions are found to be second-order saddle points for the migration of $O_i$ along the yellow channel, while $O_{i_{10}}$ has a negative Hessian eigenvalue with the eigenvector orthogonal to the channel axis. The $i_2$ interstitial, being the one with the highest co-ordination index (6 O, 6 Ga) and a strong electrostatic repulsion of about 8 eV, is calculated to have the highest formation energy. An interesting feature is noticed here for the $i_7$ site. It originates from the yellow channel and evolves to the regular $O_{II}$ position, common to the black and yellow channels, pushing $O_{II}$ to the $i_8$ site.

The $O_{i_8}$ site is the absolute minimum along the black channel by more than an eV, a result that deserves some explanation. In fact, the electron density minimum position is much closer to the center of the channel (i.e., the $i_4$ position) than the final optimized position. $O_{i_8}$ comes to lie al-

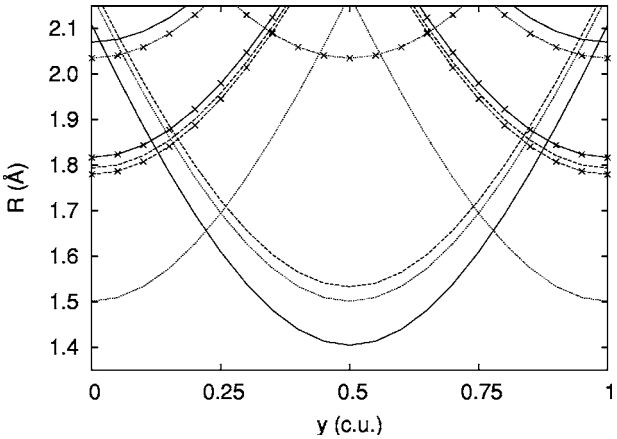


FIG. 4. Distance to several O (lines) and Ga (lines and ×) neighbors for an atom traveling along the central axis of each of the three channels defined in Fig. 2: yellow (dashed), black (solid), and red (dotted).

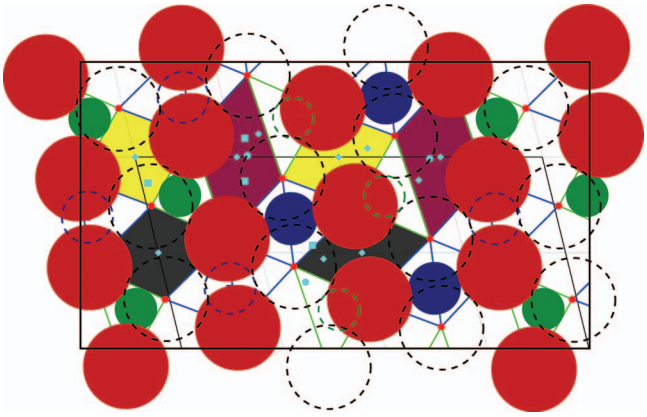

FIG. 5. (Color) A unit cell view along the $b$ axis shows the coordination polyhedra in which ions are superimposed. At $y=0$, oxygen, tetrahedral Ga, and octahedral Ga are shown by red, green, and blue, respectively. Atoms at $y=1/2$ are shown with empty dashed circles. The radii of ions are taken from Table X, later.

most in the middle of an $O_{III}$ stack along the $b$ axis, at position $(0.175,n,0.572)$ (with $n$ being an integer), which is in the corner of both the black and red channels. With a minimal lattice distortion, $O_{i_8}$ acquires a three-fold, almost planar, coordination with the nearby $Ga_{II}$ and the $Ga_I$ above and below, with a Ga-O distance of 1.84 Å. Thus, this is a true interstitial position, a hole in the structure that gets filled by an O ion without much reordering. Along the center of the black channel, the $i_4$ position is the highest in energy, and $i_3$ is the lowest in energy. Given the low-energy position found at $O_{i_{10}}$, we have also tried an intermediate $O_{i_{11}}$ position, which in this case is again the lowest along the channel. Also, $O_{i_{11}}$ is a first-order saddle point, while $O_{i_3}$ and $O_{i_4}$ are second-order saddle positions, connecting two $O_{i_{11}}$ along the $b$ axis, and two $O_{i_9}$ positions or two $O_{i_8}$ positions, respectively, for in-plane migrations. Finally, $O_{i_6}$ is also a saddle point connecting two $O_{i_8}$ minima through the kickout of an $O_{III}$ in the lattice.

The calculated results find $O_{i_8}$ and $O_{i_9}$ to be the only true minima for oxygen interstitials, while all of the rest either evolve into one of these two, or are saddle points of different orders. Let us recall that the $i_8$ and $i_9$ positions were included in the list as minima of the electron density, supporting the proposed strategy. $i_9$ was in fact the absolute minimum of $\rho$, and the site with the lowest absolute value of the electrostatic potential. $O_{i_8}$, on the other hand, started at a low-density $\rho$ minimum, but it found a better suited position by slightly distorting the lattice along the **b** axis during the optimization, a fact that no static analysis can foresee. It is, however, remarkable that simple arguments, like the distance to nearest neighbors coming from Table IV, can provide the guidance for the ordering of the energetics. In the yellow and black channels, the largest nearest-neighbor distance is around $y=0.2$, while the low-energy sites along the axis are $O_{i_{10}}$ and $O_{i_{11}}$. Nevertheless the complete picture needs all of the elements; $y=0.25$ would be the energetically favored position along the red channel according to the distance criteria, but it is in fact the $O_{i_9}$ position that is the minimum, due to its association with the low electron density and significantly less negative electrostatic potential.

TABLE VI. The calculated formation energy of the interstitial oxygen at several positions in $\beta$-$Ga_2O_3$. The energy saddle points are labeled with a †, and the so-called complex defects are labeled with an ∗.

| Defect | Position | $\Delta E_f$ (eV) | $R_{nn}$ (Å) | $I_c$ |
|---|---|---|---|---|
| Yellow channel | | | | |
| $O_{i_1}^{\dagger}$ | (0,0,0) | −11.8 | 1.64 | 2 |
| $O_{i_2}^{\dagger}$ | (0,0.5,0) | −11.5 | 2.23 | 6 |
| $O_{i_7} \rightarrow O_{i_8}$ | | | | |
| $O_{i_{10}}^{\dagger}$ | (0,0.230,0) | −12.1 | 2.01 | 4 |
| Black channel | | | | |
| $O_{i_3}^{\dagger}$ | (0,0,0.5) | −12.2 | 1.61 | 2 |
| $O_{i_4}^{\dagger,*}$ | (0,0.5,0.5) | −11.7 | 2.35 | 6 |
| $O_{i_8}$ | (0.156,0.5,0.654) | −13.4 | 1.84 | 3 |
| $O_{i_{11}}^{\dagger}$ | (0,0.205,0.5) | −12.3 | 2.06 | 4 |
| Red channel | | | | |
| $O_{i_5}^{\dagger,*}$ | (0.25,0.25,0) | −14.4 | 2.15 | 4 |
| $O_{i_9}^{*}$ | (0.277,0,0.008) | −14.5 | 2.07 | 4 |
| $O_{i_6}^{\dagger,*}$ | (0.25,0.25,0.5) | −12.0 | 1.63 | 2 |

The optimum configurations obtained for the Ga interstitials are given in Table VII. Although most of the suggested interstitial sites were suitable for oxygen ions, they do not provide favorable conditions to gallium ions. The optimized configurations of the Ga interstitials come out to be of complex nature. Except for the $i_2$ and $i_4$ positions that are associated with high formation energies, most of the configurations consist of an aggregate of more than one defect due to the large distortions in the lattice. The most stable site is found to be the $Ga_{i_8}$ site, consisting of two vacancies and three interstitials with the respective coordination indices of 5, 4, and 4. The average nearest neighbor distances of the Ga interstitials are 1.937, 1.794, and 1.802 Å in the lattice. Besides the Ga interstitials at (0.117,0.5,0.461), (0.245,0.5,0.126) in the red channel, and (0.484,0.5,0.136) in the yellow channel, there are vacancies at (0.154,0.5,0.313) associated with $V_{Ga_{II}}$ and (0.411,0.5,0.202) associated with $V_{Ga_I}$. Thus, the most stable site can be viewed in three different ways: (i) a $Ga_{i_8}$ which kicks out a $Ga_{II}$ into the red channel, which then pushes a $Ga_I$ into the yellow channel; (ii) a $Ga_i$ in the red channel pushing $Ga_I$ and $Ga_{II}$ into the yellow and black channel, respectively; or (iii) a $Ga_i$ in the yellow channel kicking $Ga_I$ into the red channel which then pushes $Ga_{II}$ into the black channel. The most stable interstitial is therefore connected to interstitials of all the three channels, which are shown in Figs. 2 and 5.

Apart from the most stable complex occurring as a multichannel minimum, the calculations also find energy minima in each channel, which are $Ga_{i_1}$, $Ga_{i_3}$, and $Ga_{i_9}$ in the yellow, black, and red channels, respectively. All of them involve bond reorganization in the lattice; $Ga_{i_1}$ displaces two $Ga_I$ into neighboring black channels, $Ga_{i_3}$ displaces two other $Ga_I$

into neighboring red channels, all of them within the $y=0$ plane, while $Ga_{i_9}$ displaces two $Ga_I$, above and below its plane, into the neighboring yellow channel. The interstitial sites $i_7$, $i_{10}$, and $i_{11}$ appear to be energetically unstable during the optimization, and stabilize to the corresponding high-symmetry positions within their channels. The only undistorted, noncomplex defects are quite high in energy. For example, $Ga_{i_2}$ is more than 1.5 eV above the lowest energy site in its channel. In fact, $Ga_{i_2}$ is at a very shallow minimum surrounded by paired saddle points that are 0.06 eV above it and at a distance smaller than 0.5 Å. Thus, $Ga_{i_2}$ can be considered as a saddle point for further calculations. Another noncomplex interstitial site, $Ga_{i_4}$, is about 3 eV above $Ga_{i_3}$ and $Ga_{i_8}$, and is indeed a saddle point of second order connecting both minima. In the red channel, $Ga_{i_5}$ is barely at a minimum, with the paired saddle points 0.3 meV above it and at a distance smaller than 0.02 Å. $Ga_{i_5}$ can therefore be considered as a saddle point, as the case with $Ga_{i_2}$. Finally, $Ga_{i_6}$ is another true saddle point associated with the highest formation energy that connects two $Ga_{i_8}$ complex minima via a kickout mechanism.

As it was the case with the oxygen interstitials, Ga interstitials seem not to be strongly affected by the electrostatic effects. Instead, the site preference for Ga interstitials seems to be driven by the short-range effects that prefer sites with appropriate oxygen coordination, even though a Ga ion has to be kicked out of its site. On the other hand, the noncomplex $Ga_{i_2}$ and $Ga_{i_4}$ interstitials are sites greatly favored by electrostatics, but with high formation energies. It seems that these two positions persist as noncomplex sites due to their electrostatically favored nature; however, in all other positions the electrostatically unfavored nature drives the formation of complex defects, which end up with a much lower energy. Thus, a complex defect configuration is likely to be the preferred configuration for Ga interstitials in $\beta$-$Ga_2O_3$.

In the present study, it is often the case that, because of the low symmetry of the monoclinic lattice, a missing atom or an interstitial distorts the lattice up to the point that a neighboring atom (e.g., oxygen) moves into one of the channels [e.g., the wider and electrostatically favored $(1/4, y, 0)$ red channel] and bonds to the atoms located on the other side of the channel, creating a complex defect. Such complex defects are found to trigger instabilities in the lattice during defect calculations. In the case of Ga interstitials, the ion kicked out is usually a tetrahedrally coordinated $Ga_I$, and so we find it to be a structurally weaker link than the corresponding octahedral $Ga_{II}$. In the case of oxygen vacancies, it is the vertex-shared $O_{II}$ that gets displaced easier, followed by $O_I$, contained on the edge shared by two octahedra in the same stack, while $O_{III}$ is the strongest link, taking part on the edges shared by octahedra both in the same stack and with the parallel stack.

### *3. Distribution of native defects*

We now focus on the temperature-dependent statistical distribution of native defects in the lattice, knowing that there is a set of possible sites for a given class of defect ($V_O$, $V_{Ga}$, $O_i$, and $Ga_i$) in $\beta$-$Ga_2O_3$. If the concentration of a given class of defect is $x_d$, the concentration of defects at a given site $i$ at constant temperature $T$ can be written as follows:

$$x_i = x_d \frac{g_i e^{-E_i/k_B T}}{q_d(T)}, \tag{4}$$

where $g_i$ is the number of sites of type $i$ per unit cell, and $k_B$ is Boltzmann's constant. $q_d(T)$ is a molecularlike canonical partition function for defects of class $d$, and is given by

$$q_d(T) = \sum_i g_i e^{-E_i/k_B T}. \tag{5}$$

Thus, $x_d = \Sigma_i x_i$. The average energy of the distribution of defects of class $d$ at temperature $T$ is given by the well-known equation

$$\langle E_d \rangle = -k_B \left( \frac{\partial \ln q_d}{\partial 1/T} \right). \tag{6}$$

This equation can be rearranged into $\langle E_d \rangle = E_0 + f_d(T)$, where 0 represents the site associated with the lowest formation energy within class $d$, and $f_d(T)$ is a single temperature-dependent function for all sites of class $d$. $f_d(T)$ is a positive-definite function, which goes to zero at zero temperature, and is shown in Fig. 6 for the native defect classes computed here. The correction term is small for the temperature range in which the ionic conductivity dominates for the defect classes. It can therefore be neglected at low temperatures, suggesting that an overwhelming majority of defects of each class will occupy the sites associated with the lowest formation energies.

Since the crystal is electrically neutral, defects must occur in the lattice with a definite stoichiometry, which is usually interpreted in terms of defects like Frenkel pairs or Schottky

TABLE VII. The calculated formation energy of the interstitial gallium ions at several positions in $\beta$-$Ga_2O_3$. The energy saddle points are labeled with a †, and the complex defects are labeled with an ∗.

| Defect | Position | $\Delta E_f$ (eV) | $R_{nn}$ (Å) | $I_c$ |
|---|---|---|---|---|
| Yellow channel | | | | |
| $Ga_{i_1}^{*}$ | (0,0,0) | −39.5 | 1.95 | 6 |
| $Ga_{i_2}^{\dagger}$ | (0,0.5,0) | −37.8 | 1.93 | 6 |
| $Ga_{i_7} \rightarrow Ga_{i_2}$ | | | | |
| $Ga_{i_{10}} \rightarrow Ga_{i_1}$ | | | | |
| Black channel | | | | |
| $Ga_{i_3}^{*}$ | (0,0,0.5) | −40.2 | 1.96 | 6 |
| $Ga_{i_4}^{\dagger}$ | (0,0.5,0.5) | −37.2 | 2.02 | 6 |
| $Ga_{i_8}^{*}$ | (0.117,0.5,0.461) | −40.7 | 1.94 | 5 |
| $Ga_{i_{11}} \rightarrow Ga_{i_3}$ | | | | |
| Red channel | | | | |
| $Ga_{i_5}^{\dagger,*}$ | (0.25,0.25,0) | −39.4 | 2.00 | 6 |
| $Ga_{i_9}^{*}$ | (0.281,0,0.099) | −39.7 | 1.92 | 5 |
| $Ga_{i_6}^{\dagger,*}$ | (0.25,0.25,0.5) | −36.1 | 1.99 | 6 |

defects. In the case of $\beta$-$Ga_2O_3$, the energies required to form Frenkel pairs and the Schottky defect are listed in Table VIII. As discussed previously, the site with the lowest formation energy of each defect class, namely $V_{O_{III}}$, $O_{i_9}$, $V_{Ga_{II}}$, and $Ga_{i_8}$, dominates the equilibrium at the temperatures considered, and so it will be chosen for subsequent calculations. It is readily apparent that the anionic Frenkel pairs are preferred for the lattice. Table VIII also lists the energies for the interconversion reactions of defects among the different sites of each class. These energies are used in the calculation of the $f_d(T)$ functions presented in Fig. 6, and they will also be useful for the migration of defects.

### B. Dopants: Formation energy and site preference

Dopants in $\beta$-$Ga_2O_3$ may be incorporated either at substitutional or interstitial sites in the lattice. Since the blue and green photoluminescent emissions in $\beta$-$Ga_2O_3$ appear to be related to cation impurities, we have considered the incorporation of divalent (Be, Mg), trivalent (In, Cr), and tetravalent (Si, Ge, Sn, Zr) ions in the lattice in the MO, $MO_3$, and $MO_2$ stoichiometries, respectively. We will first discuss the site preference for substitutional sites, then for interstitial sites, and finally we will compare the dopant inclusion at substitutional and interstitial sites.

Table IX presents the calculated formation energies of substitutional dopants in $\beta$-$Ga_2O_3$. Here, we do not expect the electrostatic potential to play a major role in the dopants' preference among the two lattice sites, I and II: the potentials are quite similar (−35.14 and −35.04 V, respectively), and the size mismatch will make the short-range contribution more important. Except for $Be^{+2}$, where the nearest-neighbors repel each other significantly at the octahedral site (see below), all other dopants prefer the octahedral $Ga_{II}$ site rather than the tetrahedral $Ga_I$.

The preferred site occupancy for $In^{+3}$ and $Cr^{+3}$, which are isovalent with $Ga^{+3}$, can be well explained from the size arguments. $In^{+3}$, being larger than $Ga^{+3}$, prefers substituting $Ga_{II}$ in the lattice, with a higher coordination index and a larger nearest-neighbor distance. Although $Cr^{+3}$ has a slightly larger ionic radii relative to $Ga^{+3}$, its short-range interaction with the oxide ion (see Fig. 1) is more repulsive, leading again to a preference for substitution at the octahedral $Ga_{II}$ site.

The doubly charged $Be^{+2}$ and $Mg^{+2}$ ions substituting $Ga^{+3}$ introduce a negative effective charge in the lattice. Hence, these substitutions are electrostatically unfavored. Nevertheless, among these two sites, there will be a slight electrostatic preference (0.1 eV) for the $Ga_{II}$ site associated with a higher potential. This is followed by $Mg^{+2}$, which being larger in size than $Ga^{+3}$, would anyway prefer the octahedral site. $Be^{+2}$, on the other hand, prefers the $Ga_I$ site. This is consistent with the general rule that a small cation needs a small coordination index. Due to the small atomic radius of $Be^{+2}$, the first neighbors are too close to each other in the octahedral coordination, thereby favoring the tetrahedral coordination with a smaller number of $O^{-2}$-$O^{-2}$ repulsions.

The tetravalent dopants substituting $Ga^{+3}$ have a positive effective charge in the lattice. However, they prefer to substitute the octahedral $Ga_{II}$ in spite of the fact that a slightly more negative value of the electrostatic potential is calculated for the $Ga_I$ site. For $Sn^{+4}$ and $Zr^{+4}$, one can explain the preferred substitutional site by noting the stronger repulsive interaction of $Sn^{+4}$ and $Zr^{+4}$ with neighboring $O^{-2}$ at the tetrahedral site. On the other hand, the site preference for $Ge^{+4}$ and $Si^{+4}$ can be explained using the coordination index, since the tetravalent dopants having a positive effective charge in the lattice would like to have a higher coordination index of oxygen.

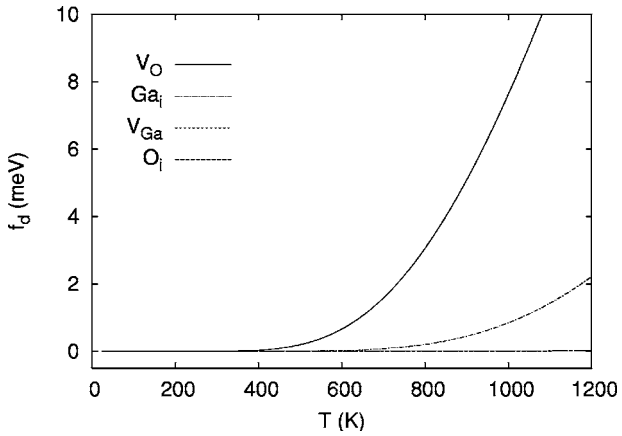


FIG. 6. The calculated temperature-dependent contributions to the average energies of each class of defects.

The lattice distortions introduced by the tetravalent dopants can be understood in terms of the ionic size and the magnitude of the electrostatic forces on the neighboring oxygen. That is, the lattice will tend to contract for all tetravalent dopants, with a further contraction/expansion effect for dopant ions that are smaller/larger than the Ga ion. For the preferred sites, tetravalent dopants always maintain the coordination index of the original lattice site with the large $Zr^{+4}$ cation as an exception. (See Tables X and XI.)

In summary, we can say that the site preference for the dopant cations substituting the Ga ion in $\beta$-$Ga_2O_3$ is driven by three factors, namely the size effect, strength of short-range repulsion, and the coordination index. The reason behind the nonproportionality of the formation energies for substitutional dopants with the electrostatic contribution is that substitutional formation energies compare the energies of two different ions at the same site, with their own different charges and short-range repulsions, whereas in the vacancies they compare the presence or absence of a single ion, with a single type of interaction.

Let us now compare the different interstitial sites. The interstitial dopants in $\beta$-$Ga_2O_3$ seem to prefer the $i_8$ site, as was the case with the host cation, $Ga_i$. In all cases including $Ga_{i_8}$, the defect configuration is in fact a complex one, in which the dopant interstitial displaces a $Ga_{II}$ from its perfect lattice location to the $i_9$ site. The resulting configuration can then be written as $M_{i_8}+V_{Ga_{II}}+Ga_{i_9}$. In the case of $Sn_{i_8}$, the Sn dopant occupies the perfect lattice position, being really a complex defect $Sn_{Ga_{II}}+Ga_{i_9}$, with energy −71.2 eV. Another preferred site for dopants in the lattice is $i_3$, where the dopants tend to form complex defects. For example, In and Si

TABLE VIII. The calculated energies (eV) of relevant native defect reactions in $\beta$-$Ga_2O_3$.

| Reaction | $\Delta E_{reac}$ | | Reaction | $\Delta E_{reac}$ | |
|---|---|---|---|---|---|
| $0 \rightarrow V_{O_{III}} + O_{i_9}$ | $E_F$ | 6.5 | $V_{Ga_{II}} \rightarrow V_{Ga_I}$ | $E_{I'}$ | 1.1 |
| $0 \rightarrow V_{Ga_{II}} + Ga_{i_8}$ | $E_{F'}$ | 11.5 | $O_{i_9} \rightarrow O_{i_8}$ | $E_1$ | 1.2 |
| $0 \rightarrow 2V_{Ga_{II}} + 3V_{O_{III}}$ | $E_S$ | 18.4 | $Ga_{i_8} \rightarrow Ga_{i_3}$ | $E_{1'}$ | 0.5 |
| $V_{O_{III}} \rightarrow V_{O_I}$ | $E_I$ | 0.3 | $Ga_{i_8} \rightarrow Ga_{i_9}$ | $E_{2'}$ | 1.0 |
| $V_{O_{III}} \rightarrow V_{O_{II}}$ | $E_{II}$ | 1.0 | $Ga_{i_8} \rightarrow Ga_{i_1}$ | $E_{3'}$ | 1.1 |

displace two $Ga_I$ ions to the $i_1$ position, while Cr, Sn, and Zr push $Ga_I$ ions to the $i_9$ position to form low-energy complex defects. It is remarkable that, in most of the complex defects (including the $Ga_i$ ones), the ion displaced is the tetrahedral $Ga_I$, going preferably into the red channel. This hints again at a structural weakness in the low-coordination site, triggered by nearby defects, and the special stability of the empty red channel.

Finally, let us compare the relative stabilities of dopants at substitutional and interstitial sites. Table XII presents the energies for the interconversion equilibria: $M_i + V_{Ga} \rightarrow M_{Ga}$ (i $\rightarrow$ s) and $M_{Ga} + Ga_i \rightarrow M_i + Ga_{Ga}$ (s $\rightarrow$ i). The divalent dopants are the only ones for which the s $\rightarrow$ i transformation is energetically possible, probably due to the high instability of the substitutional sites associated with the net negative charge in the lattice. However, the energy associated with the i $\rightarrow$ s transformation of $Be^{+2}$ and $Mg^{+2}$ is still more favorable than that associated with the s $\rightarrow$ i transformation. Hence all of the dopants considered here are likely to be stabilized at the substitutional cation sites in $\beta$-$Ga_2O_3$. Furthermore, except for $Be^{+2}$, which prefers a tetrahedral Ga site, the other dopants considered prefer the $Ga_{II}$ site. This prediction poses a restriction on the local geometry surrounding a given dopant, which might help in interpreting the results of the electron paramagnetic resonance and luminescence experiments.

### C. Transport properties: Migration

To investigate transport properties of the host lattice ions in $\beta$-$Ga_2O_3$, we should consider, in principle, both vacancy and interstitial mechanisms of diffusion in the lattice. However, as we have seen, interstitial atoms induce rather large deformations in the lattice, and many of the sites are not real minima but instead are saddle points for the ionic diffusion. Thus, we will mainly focus on the migration of the host lattice ions by the vacancy mechanism in $\beta$-$Ga_2O_3$. We note here that migration via a vacancy involves displacement of a real atom from an occupied lattice site into an empty vacancy site, which has the same effect as the displacement of the vacancy in the opposite direction.

We define the activation energy of migration ($E_j^m$) to be the energy of the saddle-point configuration relative to the isolated vacancy. The saddle point should be of first order, that is, the energy should be a maximum along the migration path but a minimum in all other directions. This is a transition state that would be located by searching along the path of migration with consideration of local symmetry characteristics.

To calculate $E_j^m$ associated with $V_O$ defects, the vacancy migration paths will be classified into two groups. In the unit cell of $\beta$-$Ga_2O_3$, the oxygen ions form connected tetrahedra ($T_d$—coordinated to $Ga_I$ ions) and octahedra ($O_h$—coordinated to $Ga_{II}$ ions), which define the empty channels labeled as yellow (y), black (b), and red (r) in Fig. 2. The first group consists of migration paths in which a lattice $O^{-2}$ will migrate to a vacancy site along the edges of the Ga coordination polyhedra, namely $T_d$ or $O_h$. Meanwhile, in the second group, we will consider the diagonal paths through the empty interstitial positions in the yellow, black, and red channels. We will label the migration paths according to the site traversed by each of them. The first part of Table XIII collects the calculated saddle points for all the possible paths of migration of the oxygen ion by the vacancy mechanism in $\beta$-$Ga_2O_3$. The activation energy of migration will be obtained by subtracting the energy of the initial vacancy site from the energy of the saddle point, and thus there will be different activation energies for asymmetric paths connecting two different vacancies.

The migration path associated with the lowest activation energy for the $O_I$ vacancy is through the red channel, that for the $O_{II}$ vacancy goes through the black channel, and that for the $O_{III}$ vacancy passes through $i_6$ while traversing the shared edge of two octahedra that connects the two octahedra stacks. For the migration path involving $O_I$-$O_{II}$ and $O_{II}$-$O_{III}$ vacancies, the preferred paths involve traversing a tetrahedron edge. On the other hand, the preferred migration path associated with the $O_I$-$O_{III}$ vacancies goes through the shared edge of two octahedra in the same stack.

Several ideas can be extracted from the preferences predicted for the migration of oxygen via the vacancy mechanism in the lattice. First, traversing coordination polyhedra edges is lower in energy than going through interstitial sites for oxygens. This is due to the fact that oxygen remains bonded to the Ga ion at the center of the polyhedron during migration along the path in the former case, while oxygen has to break the bonds in the initial configuration for the

TABLE IX. The calculated formation energy of cation dopants at substitutional sites in $\beta$-$Ga_2O_3$, together with the variation in the nearest-neighbor distance with respect to that in the perfect lattice ($\Delta R_{nn}$), and the coordination index of the dopant.

| Defect | $\Delta E_f$ (eV) | $\Delta R_{nn}$ (Å) | $I_c$ | Defect | $\Delta E_f$ (eV) | $\Delta R_{nn}$ (Å) | $I_c$ |
|---|---|---|---|---|---|---|---|
| $Be^{+2}_{Ga_I}$ | 17.5 | −0.12 | 4 | $Si^{+4}_{Ga_I}$ | −50.8 | −0.14 | 4 |
| $Be^{+2}_{Ga_{II}}$ | 18.3 | +0.01 | 6 | $Si^{+4}_{Ga_{II}}$ | −53.7 | −0.24 | 6 |
| $Mg^{+2}_{Ga_I}$ | 23.9 | +0.14 | 4 | $Ge^{+4}_{Ga_I}$ | −45.6 | +0.00 | 5 |
| $Mg^{+2}_{Ga_{II}}$ | 23.2 | +0.09 | 6 | $Ge^{+4}_{Ga_{II}}$ | −48.6 | −0.16 | 6 |
| $In^{+3}_{Ga_I}$ | 4.1 | +0.34 | 5 | $Sn^{+4}_{Ga_I}$ | −30.7 | +0.27 | 6 |
| $In^{+3}_{Ga_{II}}$ | 2.1 | +0.15 | 6 | $Sn^{+4}_{Ga_{II}}$ | −33.3 | +0.05 | 6 |
| $Cr^{+3}_{Ga_I}$ | 6.0 | +0.39 | 5 | $Zr^{+4}_{Ga_I}$ | −16.7 | +0.49 | 5 |
| $Cr^{+3}_{Ga_{II}}$ | 4.1 | +0.19 | 6 | $Zr^{+4}_{Ga_{II}}$ | −18.9 | +0.33 | 7 |

TABLE X. Shannon tetrahedral ($r_4$) and octahedral ($r_6$) effective ionic radii for the ions involved in this study.

| Ion | $r_4$ (Å) | $r_6$ (Å) | Ion | $r_4$ (Å) | $r_6$ (Å) |
|---|---|---|---|---|---|
| $Ga^{+3}$ | 0.61 | 0.76 | $O^{-2}$ | 1.24 | 1.26 |
| $Be^{+2}$ | 0.41 | 0.59 | $Si^{+4}$ | 0.40 | 0.54 |
| $Mg^{+2}$ | 0.80 | 0.86 | $Ge^{+4}$ | 0.53 | 0.67 |
| $In^{+3}$ | 0.76 | 0.94 | $Sn^{+4}$ | 0.69 | 0.83 |
| $Cr^{+3}$ | 0.66[a] | 0.76 | $Zr^{+4}$ | 0.73 | 0.86 |

[a]Estimate from $r_4/r_6$ for $Cr^{+4}$

latter case. The $O_h$ and $T_d$ paths that connect same-type oxygens are exceptions, because they involve a (0, 1, 0) displacement crossing an atomic plane halfway. The $T_d$ edges, which are not shared with other polyhedra, tend to be easy to traverse. The $O_h$ edges that are shared by two octahedra lead to a small saddle point energy, since the midpoint is exactly in between the two $Ga_{II}$ ions. If, instead of focusing into the saddle point energy, we look into the activation energies of migration, the lowest barrier of about 0.52 eV is that for the migration of $V_{O_{II}}$ to $V_{O_I}$. It is followed by the migration path involving $V_{O_{III}}$ symmetric vacancies with an activation energy of 0.67 eV.

Table XIII, later, also lists the possible paths for the migration of gallium vacancies considered in the present study. We note that the gallium ions in the lattice are surrounded by the nearest-neighbor oxygen, forming tetrahedra and octahedra. In order to migrate in the lattice, Ga ions must exit from the original coordination polyhedron through a face or an edge. Also, they have to pass through one of the empty channels, since the polyhedra share corners, with an exception of two edges being shared between octahedra. The migration paths that do not traverse the channels will be labeled as (i) $T_d$ or $O_h$ representing the migration paths along the $y$ axis in the tetrahedron or octahedron stacks; (ii) $i_6$ connecting two octahedra sharing an edge whose center is at $i_6$, and (iii) $y/b$ connecting a tetrahedron through an edge and an octahedron through a face almost in between the yellow and black channels in the lattice.

The low-energy saddle points for the migration of Ga vacancies are found to be those (i) connecting $V_{Ga_I}$ vacancies through the yellow and black channel, (ii) connecting $V_{Ga_I}$ through the red channel to $V_{Ga_{II}}$, and (iii) connecting $V_{Ga_{II}}$ vacancies along an octahedra stack. All of these paths display a double-saddle scheme (i.e., a minimum in the middle part surrounded by two maxima). This is consistent with the fact that, for the paths crossing channels, the first saddle point corresponds to Ga ions leaving the coordination polyhedron to enter into the channel, and the second to Ga ions entering the second polyhedron from the channel. The calculated double saddle points are symmetrical, since the midpoint is a high symmetry position, except for the $V_{Ga_I}$-$V_{Ga_{II}}$ path traversing the red channel. Here, there are two saddle points along the path that are associated with the exit of Ga ions from the two coordination polyhedra. Table XIII lists only the high-energy saddle point associated with Ga ions leaving the octahedron.

TABLE XI. Formation energy of interstitial impurities in $\beta$-$Ga_2O_3$. Sites marked with an $*$ correspond to complex defects.

| Defect | $\Delta E_f$ (eV) | $R_{nn}$ (Å) | $I_c$ | Defect | $\Delta E_f$ (eV) | $R_{nn}$ (Å) | $I_c$ |
|---|---|---|---|---|---|---|---|
| $Be_{i_8}^{+2}*$ | −27.3 | 1.66 | 4 | $Si_{i_3}^{+4}*$ | −92.3 | 1.77 | 6 |
| $Be_{i_{10}}^{+2}$ | −27.2 | 1.64 | 4 | $Si_{i_2}^{+4}$ | −91.7 | 1.75 | 6 |
| $Be_{i_7}^{+2}$ | −27.0 | 1.65 | 4 | $Si_{i_8}^{+4}*$ | −91.3 | 1.73 | 5 |
| $Mg_{i_9}^{+2}$ | −19.2 | 2.04 | 5 | $Ge_{i_8}^{+4}*$ | −86.4 | 1.96 | 7 |
| $Mg_{i_8}^{+2}*$ | −19.1 | 2.08 | 5 | $Ge_{i_9}^{+4}$ | −85.9 | 1.86 | 6 |
| $Mg_{i_3}^{+2}$ | −18.9 | 2.01 | 6 | $Ge_{i_2}^{+4}$ | −84.3 | 1.84 | 6 |
| $In_{i_8}^{+3}*$ | −37.5 | 2.24 | 7 | $Sn_{i_3}^{+4}*$ | −71.4 | 2.06 | 6 |
| $In_{i_9}^{+3}$ | −36.2 | 2.22 | 7 | $Sn_{i_9}^{+4}$ | −70.0 | 2.12 | 7 |
| $In_{i_3}^{+3}*$ | −35.0 | 2.13 | 6 | $Sn_{i_1}^{+4}*$ | −69.1 | 2.05 | 6 |
| $Cr_{i_8}^{+3}*$ | −35.4 | 2.26 | 6 | $Zr_{i_8}^{+4}*$ | −56.5 | 2.35 | 7 |
| $Cr_{i_9}^{+3}$ | −34.0 | 2.26 | 7 | $Zr_{i_3}^{+4}*$ | −55.8 | 2.38 | 8 |
| $Cr_{i_1}^{+3}*$ | −33.5 | 2.17 | 6 | $Zr_{i_9}^{+4}$ | −54.6 | 2.36 | 7 |

The calculated activation energies for migration show that the preferred paths are those in which a tetrahedral Ga ion migrates into the empty channels along the $(x,0,z)$ plane. The barrier heights are 0.11, 0.29, and 0.19 eV for the migration paths via the yellow, black, and red channels, respectively. The results again predict that the $GaO_4$ tetrahedra are easier to distort than the $GaO_6$ octahedra in the lattice, as pointed out earlier.

### D. Transport properties: Conductivity

The changes in the ionic conductivity of an ionic crystal with temperature involve several Arrhenius-like steps corresponding to different dominant mechanisms in the lattice.[46] For a mechanism $j$ where defect $i$ transforms into defect $i'$ (within the same class, but at a different site), the pseudoactivation energy can be expressed as

$$E_j^a = -k_B\left(\frac{\partial \ln x_i}{\partial 1/T} + \frac{\partial \ln(T\mu_j)}{\partial 1/T}\right) = E_i^c + E_j^m, \tag{7}$$

where $x_i$ is the concentration of defects at the initial site, and $\mu_j$ is the mobility associated with mechanism $j$. $E_j^m$ is the mobility contribution, and is given by the energy barrier computed for the $j$ migration path. $E_i^c$ is a concentration correction to the activation energy which, as presented in Ref. 46, can be obtained by solving a set of equations involving the Frenkel and Schottky defect formation energies. However, owing to the existence of different competing sites for each class of defect in $\beta$-$Ga_2O_3$, there is a temperature-dependent distribution that will affect the calculated results.

Taking the appropriate derivative in Eq. (4), and using the definition in Eq. (7), both for site $i$ and the general class of defects $d$, we obtain an activation energy correction for each different site in the lattice,

TABLE XII. Site preference (s: substitutional, i: interstitial) for dopants in the lattice. i→s was computed using the lowest formation energy of the interstitial dopant and the formation energy of $V_{Ga_{II}}$; s→i corresponds to the lowest formation energy of the substitutional dopant and the formation energy of $Ga_{i_8}$. Energies are in eV.

| Defect | s site | i site | $\Delta E_{i\to s}$ | $\Delta E_{s\to i}$ |
|---|---|---|---|---|
| $Be^{+2}$ | I | 8 | −6.6 | −4.1 |
| $Mg^{+2}$ | II | 9 | −9.8 | −1.7 |
| $In^{+3}$ | II | 8 | −12.6 | 1.0 |
| $Cr^{+3}$ | II | 8 | −12.7 | 1.2 |
| $Si^{+4}$ | II | 3 | −13.6 | 2.1 |
| $Ge^{+4}$ | II | 8 | −14.4 | 2.9 |
| $Sn^{+4}$ | II | 3 | −14.1 | 2.5 |
| $Zr^{+4}$ | II | 8 | −14.6 | 3.0 |

$$E_i^c = E_d^c + E_i - \langle E_d \rangle = E_d^c + (E_i - E_0) - f_d(T). \quad (8)$$

Here, $(E_i - E_0)$ is the energy of the defect $i$ relative to the lowest of its class $E_0$, which is given by the interconversion reaction shown in Table VIII. The $f_d(T)$ functions include temperature effects into the activation energies. As shown in Fig. 6, their values are smaller than 0.01 eV up to 900 K, and hence they will be disregarded in what follows.

It is interesting to note here that $E_j^m$ depends on the direction of the migrations involving asymmetric paths, while $E_j^a$ does not. If we substitute $E_j^m = E_j^{\text{saddle}} - E_i$ and Eq. (8) into Eq. (7), we find that

$$E_j^a = E_d^c + (E_j^{\text{saddle}} - E_0), \quad (9)$$

which shows that $E_j^a$ only depends on the energy of the saddle point and on global properties for the class of migrating defect, but not on the initial ($i$) or final ($i'$) states.

Equation (9) can be interpreted as follows: $E_j^a$, the activation energy, is the thermal energy required for the migration of the defect along a given path. It facilitates the excitation of defects from the lowest-energy defect configuration to another within a given class [the $E_i^c$ part in Eq. (7)], and helps the defect in surmounting the migration energy barrier [the $E_j^m$ part in Eq. (7)]. The sum of both processes is the energy difference from the most stabilized defect configuration of the defect class to the saddle point configuration of the defect in the mechanism being considered. The class concentration effects are included in the term $E_d^c$, while the temperature dependence in $f_d(T)$ has been neglected.

The global concentration corrections for each defect class can be obtained using the reactions related to the lowest-energy sites (Table VIII) together with Eq. (8). For the lowest-energy sites, $E_0^c = E_d^c$ in Eq. (8), and thus

$$E_{V_O}^c + E_{O_i}^c = E_F,$$

$$E_{V_{Ga}}^c + E_{Ga_i}^c = E_{F'},$$

$$2E_{V_{Ga}}^c + 3E_{V_O}^c = E_S. \quad (10)$$

To solve this set of equations, we have to consider the equilibrium conditions for different initial conditions, as given in the Appendix.

The concentration corrections for each defect class $d$ are given in Table XIV, considering (i) $V_O$ excess, (ii) intrinsic, and (iii) $O_i$ excess conditions. Introducing these corrections into Eq. (9) gives the activation energies for the different mechanisms, comprising the $E_j^{\text{saddle}}$ values (given in Table XIII for vacancy migration mechanisms) and a class correction $(E_d^c - E_0)$, which is shown in Table XV. The activation energies themselves are also collected in Table XV. An exhaustive search was conducted to study the migration of vacancies, although only the lowest activation energy conduction mechanisms are listed. To estimate the conduction by interstitial mechanisms, we have selected a few interstitial sites that displayed a saddle point Hessian as indicators for the possible paths.

In the intrinsic region, the lowest value of $E_j^a$ (ii) comes out to be associated with the migration path connecting $O_{i_9}$ sites along the red channel. At low temperatures, the oxygen interstitial mechanism therefore dominates the ionic conductivity of the intrinsic $\beta$-$Ga_2O_3$. This is clearly due to the ease with which an atom can move along the empty and wide red channel, which is also wide for the different atomic planes that it crosses, something that was not true for the yellow or black channels (see Figs. 4 and 5). In the intrinsic region, the ionic conduction by the oxygen vacancies is also expected to be important due to the rather low activation energies. The ionic conduction by the Ga vacancies and interstitials are likely to be negligible due to their high activation energies in the intrinsic region.

As we move away to the oxygen-rich (oxygen-deficient) conditions, calculations predict the oxygen interstitial (vacancy) mediated mechanism to dominate the ionic conduction in the lattice. So, in all conditions the preferred mechanisms would be those involving oxygen. Note that the dc and ac conductivity measurements in single crystals of $\beta$-$Ga_2O_3$ show that the dominant mechanism for migration below 900 K is ionic due to the diffusion of oxygen in the lattice,[30] hence supporting our predictions.

Another important result here is the anisotropy in Ohm's law that can be inferred from the calculated $E_j^a$ results. We note that the conductivity is a second-rank tensor, with a principal axis that corresponds to the **b** vector, while the other two axes will lie in the $(x,0,z)$ plane. For oxygen-deficient conditions in which the oxygen vacancies dominate, it appears that the preferred mechanisms have either no or a very small $y$ component in the displacements (see Table XIII). Thus, the $yy$ component of the conductivity will be smaller than the in-plane components. In the intrinsic and oxygen-rich regions, the interstitial mechanism associated with oxygen dominates the ionic conductivity. It is therefore obvious that migration along the $y$ direction via the red channel will be preferred over the in-plane migration for oxygen interstitials. Thus, the calculated results predict changes in ionic conductivity under different doping conditions that are anisotropic in nature.

TABLE XIII. The preferred vacancy migrations. Displacements refer to the vacancy effective path; the real atom hopping is opposite.

| Path | Displacement | Saddle point | $E_j^{\text{saddle}}$ (eV) | Type |
|---|---|---|---|---|
| $V_{O_I}$-$V_{O_I}$ | (0,1,0) | (−0.027,0.5,0.044) | 30.0 | $O_h$ |
| $V_{O_I}$-$V_{O_I}$ | (−0.302,0,−0.224) | (0,0,0) | 24.7 | $i_1$ |
| $V_{O_I}$-$V_{O_I}$ | (−0.302,1,−0.224) | (0.0,0.5,0.0) | 32.3 | $i_2$ |
| $V_{O_I}$-$V_{O_I}$ | (0.198,0.5,−0.224) | (0.25,0.25,0) | 22.6 | $i_5$ |
| $V_{O_I}$-$V_{O_I}$ | (0.198,0.5,0.766) | (0.25,0.25,0.5) | 30.7 | $i_6$ |
| $V_{O_{II}}$-$V_{O_{II}}$ | (0,1,0) | (0.528,0.5,0.284) | 24.8 | $T_d$ |
| $V_{O_{II}}$-$V_{O_{II}}$ | (0.022,1,−0.511) | (0.407,0.464,−0.130) | 27.2 | $i_1$ |
| $V_{O_{II}}$-$V_{O_{II}}$ | (0.022,0,−0.511) | (0.470,0.085,−0.020) | 25.2 | $i_2$ |
| $V_{O_{II}}$-$V_{O_{II}}$ | (0.022,1,0.489) | (0.5,0.5,0.5) | 26.8 | $i_3$ |
| $V_{O_{II}}$-$V_{O_{II}}$ | (0.022,0,0.489) | (0.5,−0.089,0.5) | 23.7 | $i_4$ |
| $V_{O_{III}}$-$V_{O_{III}}$ | (0,1,0) | (0.844,0.5,0.366) | 24.1 | $O_h$ |
| $V_{O_{III}}$-$V_{O_{III}}$ | (0.351,0,0.144) | (1,0,0.5) | 25.5 | $i_3$ |
| $V_{O_{III}}$-$V_{O_{III}}$ | (0.351,1,0.144) | (1.012,0.251,0.589) | 29.3 | $i_4$ |
| $V_{O_{III}}$-$V_{O_{III}}$ | (−0.149,0.5,−0.856) | (0.749,0.247,0.001) | 26.5 | $i_5$ |
| $V_{O_{III}}$-$V_{O_{III}}$ | (−0.149,0.5,0.144) | (0.75,0.25,0.5) | 22.7 | $i_6/O_h$ |
| $V_{O_I}$-$V_{O_{II}}$ | (−0.139,0.5,−0.367) | (0.129,0.286,0.004) | 22.6 | $T_d$ |
| $V_{O_I}$-$V_{O_{II}}$ | (−0.162,0.5,0.143) | (0.053,0.229,0.189) | 22.8 | $O_h$ |
| $V_{O_I}$-$V_{O_{III}}$ | (0.024,0,−0.540) | (0.159,−0.067,0.129) | 22.6 | $T_d$ |
| $V_{O_I}$-$V_{O_{III}}$ | (0.174,0.5,0.316) | (0.229,0.238,0.159) | 23.0 | $O_h$ |
| $V_{O_I}$-$V_{O_{III}}$ | (0.024,0,0.460) | (0.145,0,0.313) | 22.2 | $O_h$ |
| $V_{O_{II}}$-$V_{O_{III}}$ | (−0.164,0.5,0.172) | (0.378,0.228,0.362) | 23.1 | $T_d$ |
| $V_{O_{II}}$-$V_{O_{III}}$ | (0.186,0.5,0.317) | (0.554,0.277,0.396) | 23.4 | $O_h$ |
| $V_{Ga_I}$-$V_{Ga_I}$ | (0,1,0) | (0.086,0.5,0.816) | 59.2 | $T_d$ |
| $V_{Ga_I}$-$V_{Ga_I}$ | (−0.177,0,0.405) | (0.047,0,0.857) | 53.4 | y |
| $V_{Ga_I}$-$V_{Ga_I}$ | (−0.177,0,−0.595) | (0.053,0,0.672) | 53.6 | b |
| $V_{Ga_I}$-$V_{Ga_I}$ | (0.323,0.5,0.405) | (0.234,0.327,0.991) | 57.6 | r |
| $V_{Ga_{II}}$-$V_{Ga_{II}}$ | (0,1,0) | (0.385,0.441,0.702) | 53.9 | $O_h$ |
| $V_{Ga_{II}}$-$V_{Ga_{II}}$ | (−0.191,0.5,−0.374) | (0.25,0.25,0.5) | 58.3 | $i_6$ |
| $V_{Ga_{II}}$-$V_{Ga_{II}}$ | (0.309,0,0.626) | (0.5,0,1) | 58.3 | y |
| $V_{Ga_{II}}$-$V_{Ga_{II}}$ | (0.308,0,−0.374) | (0.482,0.392,0.558) | 57.8 | b |
| $V_{Ga_{II}}$-$V_{Ga_{II}}$ | (−0.191,0.5,0.626) | (0.25,0.25,1) | 61.3 | r |
| $V_{Ga_I}$-$V_{Ga_{II}}$ | (−0.243,0.5,−0.117) | (−0.072,0.237,0.704) | 54.6 | y/b |
| $V_{Ga_I}$-$V_{Ga_{II}}$ | (0.066,0.5,0.515) | (0.084,0.206,0.992) | 54.6 | y |
| $V_{Ga_I}$-$V_{Ga_{II}}$ | (0.066,0.5,−0.485) | (0.083,0.255,0.567) | 54.7 | b |
| $V_{Ga_I}$-$V_{Ga_{II}}$ | (0.257,0,−0.111) | (0.284,0,0.762) | 53.9 | r |

## IV. SUMMARY

A detailed theoretical study of vacancies, interstitials, and dopants was performed in monoclinic $\beta$-$Ga_2O_3$. For such a low-symmetry lattice, a systematic and general procedure is proposed to identify interstitial sites and migration paths, showing how the temperature effects can be taken into account. The most prominent structural features are found to be the empty channels along the **b** direction, which have an influence on the preferred interstitial positions and migration paths for the host lattice ions in the lattice, and the perpendicular atomic sheets, controlling the vacancy migration paths. It is seen that the tetrahedral chains along the **b** axis (especially the $Ga_I$ and the vertex-shared $O_{II}$) are the weakest links of this structure; they are easily broken by neighboring defects, leading to complex defects, defect aggregation, and possibly to structural disorder. The calculated results predict the anionic Frenkel pairs consisting of the oxygen vacancy and oxygen interstitial to dominate the defect structure in the lattice. The dopants considered here are likely to be stabilized at the octahedral gallium sites, except for $Be^{+2}$, which prefers a tetrahedral gallium site in the lattice. The oxygen interstitials are predicted to be the dominant carriers in the intrinsic and oxygen-rich conditions, while it is suggested that the oxygen vacancy mechanism dominates the conductivity in oxygen-deficient conditions. This has important consequences in the anisotropy of the conductivity, since oxygen

TABLE XIV. Class concentration corrections ($E_d^c$) for several intrinsic defects under different doping conditions.

| Defect | (i) $V_O$ excess | (ii) Intrinsic | (iii) $O_i$ excess |
|---|---|---|---|
| $V_O$ | 0 | $E_F/2$ | $E_F$ |
| $O_i$ | $E_F$ | $E_F/2$ | 0 |
| $V_{Ga}$ | $\frac{1}{2}E_S$ | $E_{F'}/2$ | $\frac{1}{2}E_S-\frac{1}{2}E_F$ |
| $Ga_i$ | $E_{F'}-\frac{1}{2}E_S$ | $E_{F'}/2$ | $E_{F'}-\frac{1}{2}E_S+\frac{1}{2}E_F$ |

interstitial mechanisms tend to favor one-dimensional $(0,y,0)$ conduction along the empty channels, while oxygen vacancies prefer two-dimensional $(x,0,z)$ mechanisms within the atomic sheets.

## ACKNOWLEDGMENTS

We acknowledge helpful discussions with Julian Gale. Funding from the Spanish DGICyT Grants No. BQU2000-0466 and No. BQU2003-06553 is acknowledged. MAB and ACC wish to thank NATO, the Spanish MEC, and the Principado de Asturias CEC for scholarships supporting their stay at Michigan Technological University. ACC also wishes to thank Spanish MCyT for her Ramón y Cajal position. Munima B. Sahariah is thankful to Michigan Tech. University for supporting her as a visiting Ph.D. student.

## APPENDIX A: EQUILIBRIUM EQUATIONS ON DIFFERENT CONDITIONS

Whenever there is a set of simultaneous chemical-like reactions involving defects, the equilibrium conditions will depend on the so-called initial constraints, i.e., those of a hypothetical initial state in which the reactants are mixed but there has been no reaction yet.

To obtain the equilibrium conditions, a set of $N_r$ (linearly) independent reactions $0 \rightarrow \Sigma_i \nu_i^r A_i$, $r=1,\ldots,N_r$, must be selected. Here, $A_i$ represents the different defect species and $\nu_i^r$ their stoichiometric coefficients in reaction $r$. In our case, grouping together the different possible sites for each class of defects, and attending only to the native defects (vacancies and interstitials), two Frenkel-like reactions together with the Schottky-like one constitute the set of independent reactions:

$$0 \rightarrow V_O + O_i \quad F,$$

$$0 \rightarrow V_{Ga} + Ga_i \quad F',$$

$$0 \rightarrow 2V_{Ga} + 3V_O \quad S. \tag{A1}$$

It is customary to use de Donder's extent of reaction,[47] defined as $d\xi^r = dx_i^r/\nu_i^r$, valid for all species involved in the reaction, and where $dx_i^r$ corresponds to the infinitesimal increase or decrease in $x_i$ due to the advance of reaction $r$. Since the total increase or decrease in $x_i$ will be the sum of those due to each of the reactions, we arrive at the set of linear equations:

TABLE XV. The preferred conduction mechanisms with their concentration-corrected pseudoactivation energies. Values for interstitial mechanisms represent lower bounds to their magnitudes.

| Mechanism | Type | $E_j^a$(i) (eV) | $E_j^a$(ii) (eV) | $E_j^a$(iii) (eV) |
|---|---|---|---|---|
| $E^c_{V_O}$-$E_0$ | | −21.0 | −18.4 | −15.8 |
| $V_{O_I}$-$V_{O_I}$ | $i_5$ | 1.5 | 4.1 | 6.7 |
| $V_{O_{II}}$-$V_{O_{II}}$ | $i_4$ | 2.6 | 5.2 | 7.8 |
| $V_{O_{III}}$-$V_{O_{III}}$ | $i_6/O_h$ | 1.7 | 4.3 | 6.9 |
| $V_{O_I}$-$V_{O_{II}}$ | $T_d$ | 1.5 | 4.1 | 6.8 |
| $V_{O_I}$-$V_{O_{III}}$ | $O_h$ | 1.2 | 3.8 | 6.4 |
| $V_{O_{II}}$-$V_{O_{III}}$ | $T_d$ | 2.0 | 4.6 | 7.2 |
| $E^c_{V_{Ga}}$-$E_0$ | | −43.0 | −46.3 | −50.8 |
| $V_{Ga_I}$-$V_{Ga_I}$ | y | 10.4 | 7.1 | 2.6 |
| $V_{Ga_I}$-$V_{Ga_I}$ | b | 10.6 | 7.3 | 2.8 |
| $V_{Ga_{II}}$-$V_{Ga_{II}}$ | $O_h$ | 10.9 | 7.5 | 3.0 |
| $V_{Ga_I}$-$V_{Ga_{II}}$ | r | 11.0 | 7.6 | 3.1 |
| $E^c_{O_i}$-$E_0$ | | 19.7 | 17.1 | 14.5 |
| $O_{i_9}$-$O_{i_9}$ | r/$i_5$ | 5.3 | 2.7 | 0.1 |
| $O_{i_9}$-$O_{i_8}$ | plane | 6.4 | 3.8 | 1.2 |
| $O_{i_8}$-$O_{i_8}$ | $i_6$ | 7.8 | 5.2 | 2.6 |
| $E^c_{Ga_i}$-$E_0$ | | 43.2 | 46.5 | 51.0 |
| $Ga_{i_9}$-$Ga_{i_3}$ | plane | 3.6 | 7.0 | 11.5 |
| $Ga_{i_8}$-$Ga_{i_8}$ | r/$i_5$ | 3.7 | 7.1 | 11.6 |
| $Ga_{i_8}$-$Ga_{i_1}$ | plane | 4.0 | 7.4 | 11.9 |

$$x_{V_O} - x_{V_O,0} = \xi^F + 3\xi^S,$$

$$x_{O_i} - x_{O_i,0} = \xi^F,$$

$$x_{V_{Ga}} - x_{V_{Ga},0} = \xi^{F'} + 2\xi^S,$$

$$x_{Ga_i} - x_{Ga_i,0} = \xi^{F'}. \tag{A2}$$

To obtain the magnitude of the concentrations, $x_i$ should be substituted in the mass-action law. Alternatively, we can eliminate $\xi$'s from the above equation to obtain

$$\frac{(x_{V_O} - x_{V_O,0}) - (x_{O_i} - x_{O_i,0})}{3} = \frac{(x_{V_{Ga}} - x_{V_{Ga},0}) - (x_{Ga_i} - x_{Ga_i,0})}{2}. \tag{A3}$$

The above exact relation leads, however, to a set of nonlinear equations whose solution requires further approximations based on different conditions, such as the oxygen-rich and oxygen-deficient cases.

The calculated formation energies of native defects suggest that the anion Frenkel defect is most likely to occur in $\beta$-$Ga_2O_3$. Since we are considering only cations as dopants, the charge compensation mechanism will therefore be dominated by the oxygen ions in the lattice. Thus, in order to simplify the equilibrium conditions, we will consider both stoichiometric and nonstoichiometric oxygen-rich and oxygen-deficient conditions.

• Intrinsic: $x_{i,0}$ are assumed to be zero for the defect-free crystal. Since the Schottky reaction requires a much larger energy than that required by the Frenkel ones (see Table VIII), it is plausible to assume that $\xi^F, \xi^{F'} \gg \xi^S \simeq 0$. Then, $x_{V_O} \simeq x_{O_i}$ and $x_{V_{Ga}} \simeq x_{Ga_i}$. Thus, $E^c_{V_O} = E^c_{O_i}$ and $E^c_{V_{Ga}} = E^c_{Ga_i}$.

• Excess of MO-like defects: For a material doped with the $x_M$ concentration of a defect, all $x_{i,0}$ are zero except $x_{V_O,0} = x_M/2$. The excess of such defects in the lattice would be much larger than their formation from the intrinsiclike reactions. Hence, $x_{V_O} \simeq x_M/2$, a constant value independent of temperature leading to $E^c_{V_O} = 0$.

• Excess of $MO_2$-like defects: Here, all $x_{i,0}$ are zero, except for $x_{O_i,0} = x_M/2$. Assuming the excess of dopants with respect to intrinsic defects, we can write $x_{O_i} \simeq x_M/2$, which yields $E^c_{O_i} = 0$.

*Corresponding author. Electronic address: mblanco@mtu.edu; Departmento de Química Física y Analítica, Universidad de Oviedo, Oviedo, 33006, Spain.

†Present address: Department of Physics, Indian Institute of Technology, Guwahati, Assam, India.

‡Present address: Departmento de Química Física y Analítica, Universidad de Oviedo, Oviedo, 33006, Spain.

[1] S. Geller, J. Chem. Phys. **33**, 676 (1960).
[2] M. Passlacki, N. E. J. Hunt, E. F. Schubert, G. J. Zydzik, M. Hong, J. P. Mannaerts, R. L. Opila, and R. J. Fischer, Appl. Phys. Lett. **64**, 2715 (1994).
[3] M. Passlacki, E. F. Schubert, W. S. Hobson, M. Hong, N. Moriya, S. Chu, K. Konstadinidis, J. P. Mannaerts, M. L. Schnoes, and G. J. Zydzik, J. Appl. Phys. **77**, 686 (1994).
[4] M. Passlacki, M. Hong, E. F. Schubert, J. R. Kwo, J. P. Mannaerts, S. Chu, N. Moriya, and F. A. Thiel, Appl. Phys. Lett. **66**, 625 (1995).
[5] M. Passlacki, M. Hong, and J. P. Mannaerts, Appl. Phys. Lett. **68**, 1099 (1996).
[6] Z. Li, C. de Groot, J. Jagadeesh, and H. Moodera, Appl. Phys. Lett. **77**, 3630 (2000).
[7] E. Aubay and D. Gourier, Phys. Rev. B **47**, 15023 (1993).
[8] L. Binet and D. Gourier, J. Phys. Chem. Solids **59**, 1241 (1998).
[9] D. D. Edwards, P. E. Folkins, and T. O. Mason, J. Am. Ceram. Soc. **80**, 253 (1997).
[10] N. Ueda, H. Hosono, R. Waseda, and H. Kawazoe, Appl. Phys. Lett. **71**, 933 (1997).
[11] D. D. Edwards, T. O. Mason, F. Goutenoire, and K. R. Poeppelmeier, Appl. Phys. Lett. **70**, 1706 (1997).
[12] X. Wu, W. Song, W. Huang, M. Pu, B. Zhao, Y. Sun, and J. Du, Chem. Phys. Lett. **328**, 5 (2000).
[13] G. Park, W. Choi, J. Kim, Y. Choi, Y. Lee, and C. Lim, J. Cryst. Growth **220**, 494 (2000).
[14] W. Han, P. Kohler-Redlich, F. Ernst, and M. Rühle, Solid State Commun. **115**, 527 (2000).
[15] M. Orita, H. Ohta, and M. Hirano, Appl. Phys. Lett. **77**, 4166 (2000).
[16] C. Liang, G. Meng, G. Wang, Y. Wang, L. Zhang, and S. Zhang, Appl. Phys. Lett. **78**, 3202 (2001).
[17] J. Li, X. Chen, Z. Qiao, M. He, and H. Li, J. Phys.: Condens. Matter **13**, L937 (2001).
[18] M. Fleischer and H. Meixner, J. Appl. Phys. **74**, 300 (1993).
[19] K. Bernhardt, M. Fleischer, and H. Meixner, Siemens Forsch.-Entwicklungsber. **30**, 35 (1995).
[20] M. Marezio and J. P. Remeika, J. Chem. Phys. **46**, 1862 (1967).
[21] D. F. Edwards, in *Handbook of Optical Constants of Solids*, edited by E. D. Palik (Academic, New York, 1998), Vol. III, Chap. $\beta$-gallium oxide, p. 753.
[22] G. M. Wolten and A. B. Chase, J. Solid State Chem. **16**, 377 (1976).
[23] S. Geller, J. Solid State Chem. **20**, 209 (1977).
[24] J. Áhman, G. Svensson, and J. Albertsson, Acta Crystallogr., Sect. C: Cryst. Struct. Commun. **52**, 1336 (1996).
[25] H. H. Tippins, Phys. Rev. **140**, A316 (1965).
[26] T. Matsumoto, M. Aoki, A. Kinoshita, and T. Aono, Jpn. J. Appl. Phys. **13**, 1578 (1974).
[27] M. R. Lorenz, J. F. Woods, and R. J. Gambino, J. Phys. Chem. Solids **28**, 403 (1967).
[28] L. N. Cojocaru and I. D. Alecu, Z. Phys. Chem., Neue Folge **84**, 325 (1973).
[29] L. N. Cojocaru and A. Prodan, Rev. Roum. Phys. **19**, 209 (1974).
[30] T. Harwig, G. J. Wubs, and G. J. Dirksen, Solid State Commun. **18**, 1223 (1976).
[31] E. Víllora, T. Atou, T. Sekiguchi, T. Sugawara, M. Kikuchi, and T. Fukuda, Solid State Commun. **120**, 455 (2001).
[32] T. Harwig, F. Kellendonk, and S. Slappendel, J. Phys. Chem. Solids **39**, 675 (1978).
[33] R. Stalder and K. H. Nitsch, J. Am. Ceram. Soc. **80**, 258 (1997).
[34] C. R. A. Catlow and W. C. Mackrodt, in *Computer Simulation of Solids*, Lecture Notes in Physics, edited by C. R. A. Catlow and W. C. Mackrodt (Springer-Verlag, Berlin, 1982).
[35] R. Pandey, J. D. Gale, S. K. Sampath, and J. M. Recio, J. Am. Ceram. Soc. **82**, 3337 (1999).
[36] P. Zapol, R. Pandey, and J. D. Gale, J. Phys.: Condens. Matter **9**, 9517 (1997).
[37] P. Zapol, R. Pandey, M. Ohmer, and J. D. Gale, J. Appl. Phys. **79**, 671 (1996).
[38] J. D. Gale, J. Chem. Soc., Faraday Trans. **93**, 629 (1997).
[39] T. S. Bush, J. D. Gale, C. R. A. Catlow, and P. D. Battle, J. Mater. Chem. **4**, 831 (1994).
[40] V. Luaña and L. Pueyo, Phys. Rev. B **41**, 3800 (1990).
[41] M. A. Blanco, A. Martín Pendás, and V. Luaña, Comput. Phys. Commun. **103**, 287 (1997).
[42] J. M. Recio, E. Francisco, M. Flórez, and A. Martín Pendás, J. Phys.: Condens. Matter **5**, 4975 (1993).
[43] M. A. Blanco, J. M. Recio, E. Francisco, A. Costales, V. Luaña,

and A. Martín Pendás, Radiat. Eff. Defects Solids **151**, 223 (1999).
[44] E. Clementi and C. Roetti, At. Data Nucl. Data Tables **14**, 177 (1974).
[45] A. Martín Pendás, A. Costales, and V. Luaña, Phys. Rev. B **55**, 4275 (1997).
[46] H. Jiang, A. Costales, M. A. Blanco, M. Gu, R. Pandey, and J. D. Gale, Phys. Rev. B **62**, 803 (2000).
[47] D. Kondepudi and I. Prigogine, *Modern Thermodynamics* (Wiley, Chichester, England, 1998).